1.4 million Q factor Si$_3$N$_4$ micro-ring resonator at 780 nm wavelength for chip-scale atomic systems

Martin Sinclair,[1,2] Kevin Gallacher,[1] Marc Sorel,[1] Joseph C. Bayley,[2] Euan McBrearty,[1] Ross W. Millar,[1] Stefan Hild,[2] and Douglas J. Paul[1,*]

[1] *University of Glasgow, James Watt School of Engineering, Rankine Building, Oakfield Avenue, Glasgow, G12 8LT, UK*
[2] *University of Glasgow, School of Physics and Astronomy, Kelvin Building, University Avenue, Glasgow, G12 8GG, UK*
*Douglas.Paul@glasgow.ac.uk

Abstract: A silicon nitride micro-ring resonator with a loaded Q factor of 1.4×10^6 at 780 nm wavelength is demonstrated on silicon substrates. This is due to the low propagation loss waveguides achieved by optimization of waveguide sidewall interactions and top cladding refractive index. Potential applications include laser frequency stabilization allowing for chip-scale atomic systems targeting the ^{87}Rb atomic transition at 780.24 nm. The temperature dependent wavelength shift of the micro-ring was determined to be 13.1 pm/K indicating that a minimum temperature stability of less than ±15 mK is required for such devices for wavelength locking applications. If a polyurethane acrylate top cladding of an optimized thickness is used then the micro-ring could effectively be athermal, resulting in reduced footprint, power consumption, and cost of potential devices.

1. Introduction

High-Q factor optical micro-ring resonators have a wide range of applications such as serving as filters, delay lines and switches [1], external cavity frequency reference for diode lasers [2], integrated laser cavity coupled to a gain medium [3], source of frequency comb generation [4], source of entangled photon pairs [5], or the sensing element for resonant optical gyroscope [6]. Most high-Q factor micro-rings to date have been designed and demonstrated at telecoms wavelengths especially around 1550 nm where narrow linewidth lasers are mature and readily available. Silicon photonic devices have been pushed to Q factors as high as 1.1×10^6 [7]. Higher Q factors have been demonstrated from a range of lower refractive index materials where the losses can be reduced significantly such as silicon nitride where Q factors are now 6.7×10^7 [8] for large modal overlapping waveguides and 8.1×10^7 for low modal overlaps with waveguides [9].

For quantum technology applications such as chip-scale atomic devices [10] which include: atomic clocks [10–12], magnetometers, quantum effects metrology references [13], quantum gravimeters, and gradiometers, atomic transitions are used with wavelengths well away from the standard telecoms 1310 nm and 1550 nm. Systems that use ^{87}Rb atoms require 780.24 nm photonic components if photonics integrated circuit systems for thermal or cold atom systems are to be realized. As the wavelength is reduced, however, the scattering losses in waveguides increase significantly as a function of the inverse of the wavelength [14,15] resulting in significantly lower micro-ring Q factors close to 780 nm, see Table 1.

Table 1. A comparison of micro-ring resonators at or close to 780 nm operational wavelength.

Material platform	Wavelength (nm)	Waveguide loss (dB/cm)	micro-ring diameter (μm)	micro-ring loaded Q	Ref.
Si_3N_4	668.38		25	$(1.52 \pm 0.02) \times 10^5$	[16]
AlN	774.24	40	20	3.0×10^4	[17]
Si_3N_4	780		20	1.5×10^4	[18]
polymer	780	1.1	60	1×10^5	[19]
TiO2	780		150	1.6×10^5	[20]
Si_3N_4	**780**	**0.2**	**600**	**$(1.38 \pm 0.04) \times 10^6$**	**This work**
strip-loaded Si_3N_4	784	0.2	700	3.6×10^6	[21]
SiO_xN_y	850	0.8	200	1.3×10^5	[22]
Si_3N_4	933.62		25	$(1.04 \pm 0.02) \times 10^6$	[16]

Our long term vision is to develop a silicon nitride (Si_3N_4) photonic integrated circuit platform with all the photonic components required for thermal and cold atom chip-scale atomic systems. This platform is aimed at ^{87}Rb requiring 780.24 nm optimized photonic components including narrow linewidth lasers, polarization rotation ($\lambda/2$), polarizing beam-splitters (couplers) and phase modulators [23,24]. Previously we have demonstrated a low loss Si_3N_4 with silicon dioxide (SiO2) cladding photonic platform with integrated 780.24 nm distributed feedback lasers (DFB) lasers coupled through spot sized converters to provide over 15 mW of laser power on the chip [25,26]. To be useful for chip scale atomic devices and especially cold atom systems [12], the laser needs to be stabilized by locking to either a Rb vapor atomic transition [24] or locked to a cavity such as a micro-ring [23]. A micro-ring resonator has also been used to achieve Doppler cooling of Cesium atoms with evanescent field interactions [27].

In this work, we demonstrate micro-ring resonators with Q factors up to 1.4×10^6 at 780 nm developed in a 200 nm thick Si_3N_4 photonic platform on 150 mm diameter silicon substrates. This thickness of waveguide material has been chosen to support both TE and TM fundamental modes allowing for design of integrated polarization control and other essential integrated active and passive photonic components for thermal and cold atom systems resulting in a design criteria intermediate to the usual large [8] or small [9] waveguide modal overlapping approaches for high Q factor micro-rings.

2. Design and fabrication methods

Silicon nitride layers for waveguide cores were deposited by a low-pressure chemical vapor deposition (LPCVD) tool at 750 °C onto a 4 μm thick thermal SiO_2 layer grown by wet oxidation at 1000 °C. The waveguide pattern was written in hydrogen silsequioxane (HSQ) negative resist using electron beam lithography with a Vistec VB6 electron beam lithography tool and etched using a CHF_3/O_2 reactive ion etch. Typically HSQ is removed with hydroflouric acid which would damage the Si_3N_4 core and SiO_2 bottom cladding. In this work a sacrificial layer of poly-methyl-methacrylate (PMMA) ~50 nm is used to perform lift-off of ~360 nm HSQ, this technique has been previously established [28]. After etching, the HSQ etch mask is removed by lift-off and a SiO_2 top cladding layer can be added using plasma-enhanced chemical vapor deposition (PECVD) at 300 °C.

For moderately-confined waveguides used at relatively short wavelengths such as those presented here, it is essential that the difference in refractive index of the top and bottom cladding layers (Δn_{cl}) is not high enough to support any slab mode with low propagation loss as not only would the high index contrast result in greater scattering loss for the waveguide [14,15] but the slab mode formed due to stray light from the laser in-coupling would raise the noise floor,

potentially obscure the mode propagating in the waveguide, and truncate the resonance peak thereby artificially decreasing the Q factor. The slab mode shown in Fig. 1(b) is for a Δn_{cl} of only 0.01. The effect seen experimentally is that the slab mode is perturbed by the waveguide features on the sample chip and so assorted higher order modes can be seen. This issue is more pronounced for shorter wavelengths than it is for telecoms wavelengths because for longer wavelengths, a top cladding layer can be much thicker before it could support a slab mode and so the index matching is less of a concern. PECVD was used to deposit the top SiO_2 cladding layer with the initial process (PECVD 1) having a refractive index much greater than a thermal oxide layer, see Fig. 1(a). This resulted in a strongly guided slab mode that obscures the waveguide mode. This deposition process was preformed at 300 °C and 900 mT with high frequency RF power 40 W, and N_2 (392 sccm), N_2O (1420 sccm), and SiH_4 (20 sccm) gases. Annealing the top SiO_2 cladding at 1100 °C was successful in reducing the refractive index.
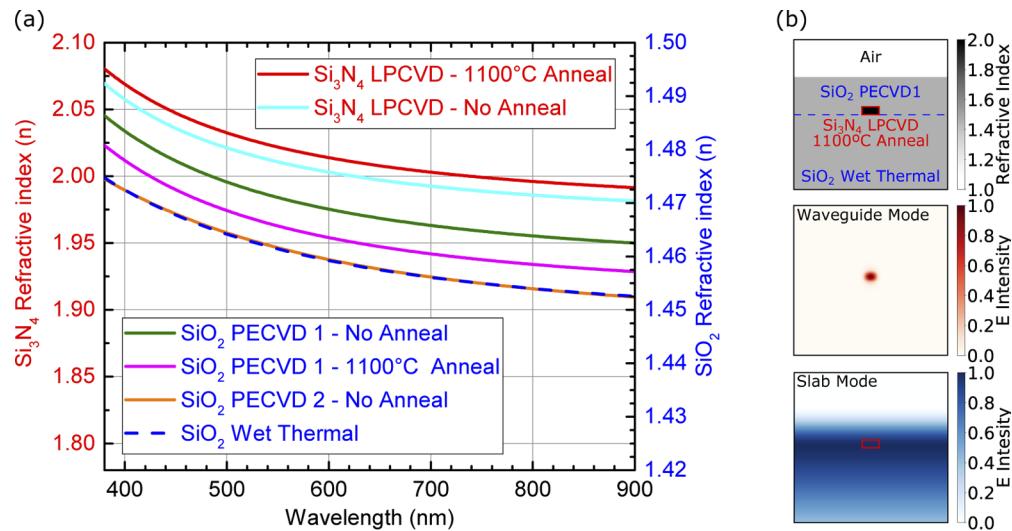

Fig. 1. (a) The refractive indices as a function of wavelength for the Si_3N_4 LPCVD (red/left axis) and SiO_2 deposition/growth (blue/right axis) were investigated. Measurements were performed using an ellipsometer and then refractive index was found by fitting a Cauchy model to the ellipsometer data. (b) Top: The refractive index profile at 780 nm wavelength for a 1100 nm wide, 200 nm high waveguide core. Middle: Simulated TE0 mode profile for the Si_3N_4 waveguide with PECVD 2 top cladding. Bottom: Simulated TE0 slab mode supported by a 1 µm thick PECVD 1 SiO_2 top cladding for finite boundary conditions with a red box to indicate the Si_3N_4 waveguide core, the difference in refractive index between the top and bottom cladding layers in this case is $\Delta n_{cl} = 0.01$. The simulation region shown in each plot is 10 µm wide and 4 µm high.

A new process (PECVD 2) was developed without the requirement for annealing to provide a refractive index close enough to that of the bottom cladding to suppress the formation of any undesired slab mode. This new deposition process was performed again at 300 °C and 2150 mTorr with high frequency RF power 550 W and only N_2O (3000 sccm), and SiH_4 (175 sccm) gases. Sample wafers were prepared with 1 µm of SiO_2 and measured using a JA Woollam M2000X spectroscopic ellipsometer to find that the PECVD SiO_2 as deposited had a refractive index of 1.454 ± 0.003 at 780 nm whilst the SiO_2 bottom cladding grown by wet thermal oxidation has a refractive index of 1.4544 ± 0.0001. The LPCVD Si_3N_4 has a refractive index of 1.987 ± 0.001 as deposited and 1.9973 ± 0.0004 after annealing at 1100 °C, see Fig. 1(a).

Waveguide cross-sectional dimensions were modeled to determine the effective index of the guided modes for different waveguide widths see Fig. 2(a). A width of 500 nm was chosen initially to be certain that only the fundamental mode was supported. However, there was no observable coupling into higher order modes for waveguide widths up to 1100 nm. All-pass micro-ring resonators were designed and fabricated for a series of gap spacing and waveguide widths both with a PECVD SiO_2 top cladding and without (i.e. air clad), see Fig. 2(b). The gap spacing between the bus waveguide and the micro-ring resonator determines the power coupling into the micro-ring resonator. For each micro-ring resonator the transmission spectra were recorded and the resonance peak attributes were determined.
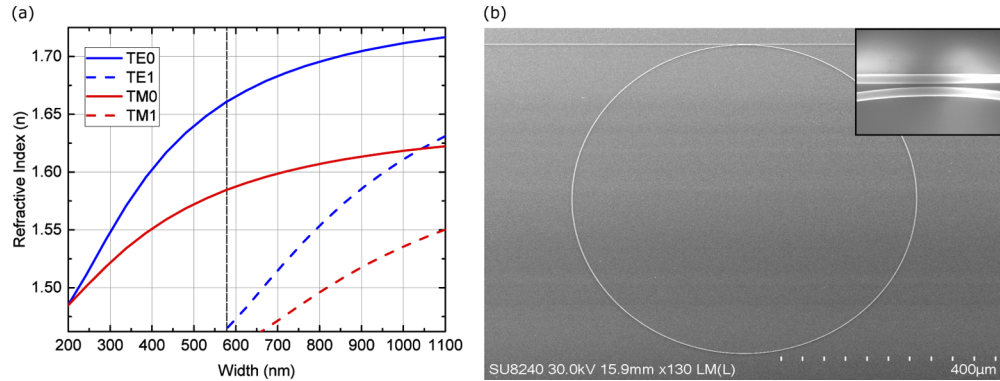

Fig. 2. (a) The effective index of fundamental and first order transverse electric (TE) and transverse magnetic (TM) modes were simulated for different waveguide widths. The TE1 mode is not supported for waveguide width <570 nm. (b) Scanning electron microscope (SEM) image shows a micro-ring resonator 300 μm radius, 1100 nm waveguide width, 200 nm thickness, with an inset close up of an evanescent coupler.

3. Method

Transmission spectra were recorded using a SolsTiS titanium sapphire laser manufactured by M Squared Lasers with tunable wavelength range from 675 nm to 1050 nm and a linewidth of <50 kHz. The laser has three internal cavities which can provide three different frequency sweeps. These have a maximum scanning range of 250 GHz (500 pm), 66 GHz (130 pm), and 30 GHz (60 pm). The smallest scanning range cavities are able to provide the highest resolution frequency sweeps. The laser beam was initially incident upon a mechanical chopper which was used in conjunction with a lock-in amplifier to reduce the noise in the signal due to ambient light detected by the photodiode. Light was fiber coupled thereafter, allowing for the use of a fiber attenuator and a fiber polarization controller, used to prevent the injection of undesired modes, before a lensed fiber is used to coupled light into the input facets of the test chip. Light exiting the chip was collected on an objective lens and focused onto both a camera, which was used for alignment, and a silicon photodiode, for recording the transmitted power. The complete setup is shown in the schematic diagram in Fig. 3.

The power transmission of light through an all-pass micro-ring resonator is described by

$$P_{\text{tran}}(\nu) = A \frac{t^2 - 2t\tau \cos\left[2\pi(\nu - \nu_{\text{res}})t_{RT}\right] + \tau^2}{1 - 2t\tau \cos\left[2\pi(\nu - \nu_{\text{res}})t_{RT}\right] + t^2\tau^2} + B(\nu) \tag{1}$$

where A is the amplitude of the power transmission peak, t is coefficient for the field amplitude transmitted through the bus waveguide (rather than coupled into the resonator), τ is the field amplitude loss of the micro-ring resonator, ν is free space frequency, ν_{res} is the resonance
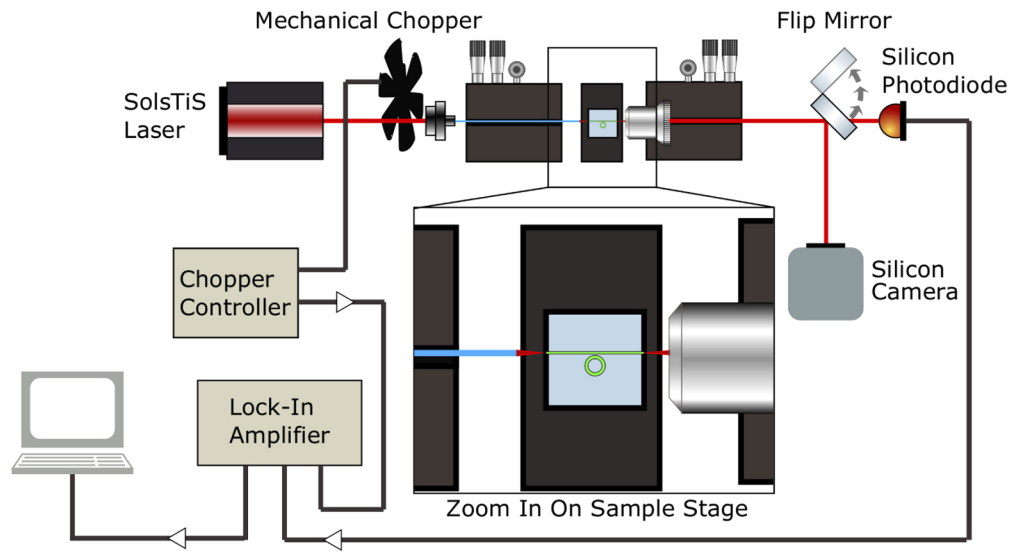
Fig. 3. Schematic diagram of micro-ring resonator optical transmission experimental setup.

frequency of the resonator, t_{RT} is the round trip time for the micro-ring resonator, and B is a background function describing the data in the absence of the resonance peak [29,30]. It has been shown that it is possible to determine the loss and power coupling of a micro-ring resonator by fitting Eq. (1) to the recorded power transmission spectra but that these values are irrevocably entangled for a single resonance measurement such as this. They could, however, be distinguished by performing measurements of a series of resonance peaks and determining which fitted parameter shows the (co)sinusoidal behavior with wavelength expected for the coupling coefficient [31]. By this method, the propagation loss is determined to be ~ 0.2 dB/cm, see Table 1, similarly an approximate power coupling of 0.4 % was determined.

Micro-ring resonators are routinely characterized by fitting a Lorentzian distribution to the resonance peak [1,3,32],

$$f(v) = -A \frac{1}{1 + \left[\frac{v - v_{res}}{\gamma}\right]^2} + B(v), \tag{2}$$

where v_{res} is the mean frequency of the distribution corresponding to the resonance frequency, γ is the half width at half maximum (HWHM). By fitting Eq. (2), via a non-linear least squares method, the essential attributes of the resonance peak can be found, see Table 2. The Q factor is defined as the ratio of the resonance peak mean position and the full width at half maximum (FWHM), $\frac{v_{res}}{2\gamma}$, and the amplitude is given by A which is also used to find the extinction ratio of the resonance peak. The peak slope gradient is determined by taking the derivative of the Lorentzian distribution and finding its maximum value, this corresponds to the side of the resonance peak. The background function used in Eqs. (1) and (2) is the second degree polynomial,

$$B(v) = b_0 + b_1(v - v_{res}) + b_2(v - v_{res})^2 \tag{3}$$

Table 2. The micro-ring resonator characteristics are determined by fitting a Lorentzian distribution to the resonance peak in the power transmission spectra using the non-linear least squares method and extracting the fit parameters.

Q (10^6)	FWHM (fm)	Mean λ (nm)	Amplitude (μW)	Extinction Ratio %
1.38±0.04	570± 20	779.9±0.8	12.3±0.2	46.8±0.6

where $b_{0,1,2}$ are coefficients of the polynomial.

4. Results

Initial experiments using 500 nm wide waveguides with and without top cladding were intended to illustrate the benefit of the top cladding layer and aid the development of future devices. A micro-ring resonator with a SiO_2 top cladding cannot be fairly compared to a micro-ring resonator with an air top cladding when the two have the same gap spacing, this is because the different index of the top cladding will significantly change the power coupled into the micro-ring resonator. In order to make a fair comparison between the SiO_2 and air clad waveguides, they are compared using the difference between the effective index of the first two eigenmodes of the coupled waveguide supermode formed by the bus waveguide and micro-ring resonator at their closest point, $\Delta n_{eff} = n_{eff1} - n_{eff2}$ [33]. Coupled mode theory can be used to show that the power coupled into the micro-ring resonators scales with this value [34,35]. This allows for a fair comparison between the SiO_2 and air clad micro-ring resonator, see Fig. 4(a) . The samples with the top SiO_2 cladding are shown in Fig. 4(a) to exhibit a Q factor about twice as great as the samples with no top cladding.
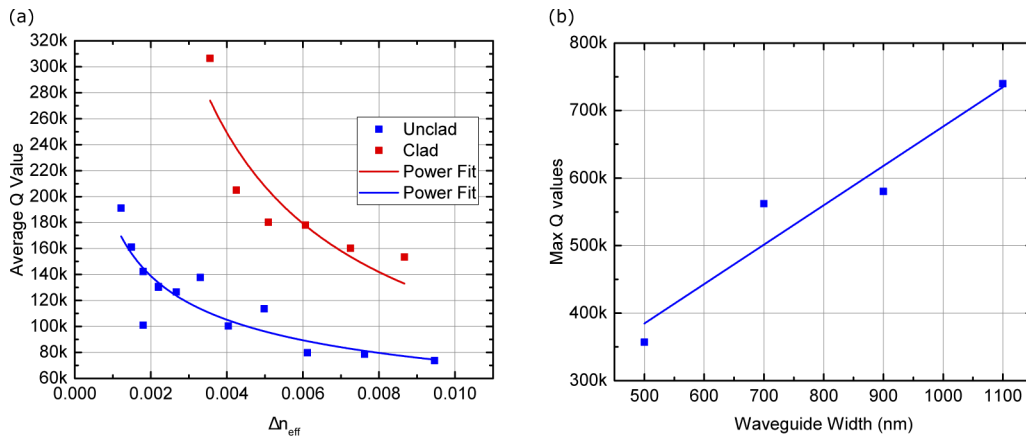

Fig. 4. Experimentally measured Q factor values for micro-rings comprised of 200 nm LPCVD Si_3N_4 waveguide core on a SiO_2 bottom cladding. (a) The average Q values against Δn_{eff}, waveguide width is 500 nm, micro-ring radius is 250 μm. (b) The maximum Q values against waveguide widths for micro-rings with no top cladding material deposited, micro-ring radius is 300 μm.

It is expected that the sidewall roughness of the waveguide core is a critical loss mechanism [14,15] and it has been shown in other work that low propagation losses can be achieved either by designing high aspect ratio waveguides such that the modal interaction with the sidewalls is minimized [36–38] or by using a SiO_2 hard mask instead of a polymer etch mask in order to reduce the roughness due to the polymer residue on the sidewall [8]. For this reason the width of the waveguides was experimentally varied and for a range of gap spacings, the best Q factor value was recorded, see Fig. 4(b) . The trend in Fig. 4(b) of Q factor increasing with waveguide widths leads to the conclusion that the limiting loss mechanism is the sidewall scattering and that higher Q factor values are achievable for wider waveguides. Results from Fig. 4(b) are for samples with no top-cladding, considering also Fig. 4(a) it is clear that the best Q values can be obtained for wider waveguides with a SiO_2 top cladding.

To achieve a Q of $(1.38\pm0.04)\times 10^6$, see Fig. 5(a), a micro-ring resonator was designed to have a Si_3N_4 core 200 nm thick and 1100 nm wide, a bottom cladding 4 μm thick, and a top

cladding 900 nm thick. The transmission spectra shown in Fig. 5(a) corresponds to a laser sweep of 30 GHz (60 pm) bandwidth around a center wavelength of 780 nm. An estimate of the error in transmitted power is found by performing the same scan with no sample in place, the background power is approximated as a straight line and subtracted from this data, the standard deviation of the result is an estimate of the noise. This uncertainty can then be propagated to the sample measurement. The micro-ring resonator characteristics found by fitting Eq. (2) are shown in Table 2. A high resolution scan is required to resolve this resonance peak, the scan in Fig. 5(a) has a resolution of 60 fm. A broadband sweep is required to measure the free spectral range (FSR) of the micro-ring resonator but the high-Q resonance peak, Fig. 5(a), cannot be resolved with the 250 GHz frequency sweep. This scan was performed on lower Q factor micro-rings with the same optical path length, an FSR of 99 ± 3 pm or 49 ± 1 GHz was found see Fig. 5(b).
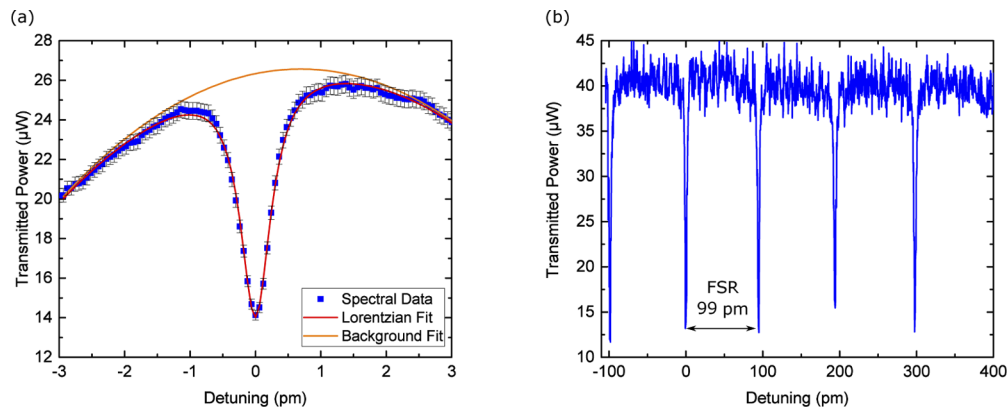

Fig. 5. The transmission spectra of micro-ring resonators. (a) A Lorentzian fit to a resonance peak with a Q value of 1.4 million, this has a Si_3N_4 core 200 nm thick and 1100 nm wide, a bottom cladding 4 μm thick, and a top cladding 900 nm thick. The blue trace is the raw data of a 30 GHz (60 pm) bandwidth transmission spectra centered on 780 nm; the orange trace is the background fit provided by a second degree polynomial; the red trace is the Lorentzian fit from Eq. (2). (b) A 250 GHz (500 pm) bandwidth transmission spectra centered on 780 nm of a lower Q micro-ring resonator with the same optical path length showing a free spectral range (FSR) of 99 pm.

All Q factor values reported in this paper are loaded Q factors including the Q factor value of 1.4×10^6 shown in Fig. 5(a). This to our knowledge is the highest Q factor value that has been reported for a buried ridge waveguide micro-ring at 780 nm wavelength (see Table 1). A higher Q factor value is recognized for strip-loaded waveguide micro-rings at 780 nm [21] wherein a thin film of Si_3N_4 acts as the waveguide core but the mode is localized instead by a strip of SiO_2 on top of the core. This strip-loaded waveguide does not require etching of the waveguide core and so avoids the sidewall scattering losses typically found to be the dominant loss mechanism in buried ridge waveguides, thereby potentially demonstrating an upper limit of Q factor for micro-ring resonators with a similar size and wavelength. However, the strip-loaded waveguides fabricated using this process [21] offer limited possibilities for integration because the addition of top cladding or any other material to the surface of the completed micro-ring resonator, for metallization or packaging, would interact with the mode which could cause optical loss. Additional waveguide cladding deposited on the surface would need to have a refractive index lower than that of SiO_2 to ensure that the waveguide mode persists which would present a significant challenge for integration. By contrast, the foundry compatible process detailed in this work provides a buried ridge waveguide with a top cladding surface that ensures that any material deposited on the surface cannot interact with the waveguide mode. If the micro-ring

resonator demonstrated in this work were to be used as a frequency reference for stabilizing a diode laser, then using the simple side locking method [23,39] , transmission spectra provides an error response of $30\,\text{nW}\,\text{fm}^{-1}$, this corresponds to an error signal of $800\,\text{nV}\,\text{fm}^{-1}$ produced by the amplified photodetector. The total actuation range is $\sim 400\,\text{fm}$ with a maximum deviation from a set point of $\pm\,200\,\text{fm}$.

5. Analysis

To ensure that the resonance wavelength is at the desired wavelength, the micro-ring resonator would have to be temperature controlled. For a waveguide comprised a bottom cladding layer, a top cladding layer, and a core. The total thermo-optic coefficient (TOC) of the waveguide is determined by Eq. (4) [40].

$$\frac{dn_{\text{eff}(\lambda)}}{dT} = \Gamma_{cr}(\lambda)\frac{dn_{\text{cr}(\lambda)}}{dT} + \Gamma_{tcl}(\lambda)\frac{dn_{\text{tcl}(\lambda)}}{dT} + \Gamma_{bcl}(\lambda)\frac{dn_{\text{bcl}(\lambda)}}{dT} \tag{4}$$

The bulk TOCs of the materials that form the waveguide are weighted by the confinement of light within those materials. The confinement factors, Γ, for each material are found by simulating the waveguide geometry in Lumerical MODE Solutions, integrating the light power propagating in those materials, and normalizing this with respect to the total power of the propagating optical mode. The group refractive index of the mode is also found using Lumerical MODE Solutions and used in Eq. (5) to find temperature dependent wavelength shift (TDWS) [40].

$$\frac{d\lambda}{dT}(\lambda) = \frac{\lambda}{n_g}\frac{dn_{\text{eff}}}{dT}(\lambda) \tag{5}$$

For the TE0 mode propagating in a waveguide width of 1100 nm, as used for Fig. 5(a), the TDWS is 13.1 pm/K. This means that in order to stabilize the temperature of the micro-ring such that the the wavelength is within the actuation range of the resonance peak, a minimum temperature stability of less than $\pm\,15\,\text{mK}$ is required. This requirement is readily achievable with a commercial thermo-electric cooler. Passive temperature stability could be realized by using a top cladding layer that would reduce the waveguide TOC.

The condition for an athermal micro-ring resonator is that $\frac{dn_{\text{eff}(\lambda)}}{dT} = 0\,\text{K}^{-1}$ which can only be achieved if the materials used have an appropriate mix of positive and negative TOCs. The TOCs of SiO_2 and Si_3N_4 are $\frac{dn_{\text{SiO}_2}(\lambda)}{dT} = 1.0 \times 10^{-5}\text{K}^{-1}$ [40,41] and $\frac{dn_{\text{Si}_3\text{N}_4}(\lambda)}{dT} = 2.5 \times 10^{-5}\text{K}^{-1}$ [40,42] respectively, so a top cladding layer must have a negative TOC and be greater in magnitude than $\sim 10^{-5}$. The TOC of polymethyl methacrylate (PMMA) was measured and found to be $-1.01 \times 10^{-4}\text{K}^{-1}$. Because PMMA has a higher refractive index (1.504 ± 0.006 at 780 nm) than SiO_2, care must be taken to suppress the formation of a slab mode in this top cladding. Considering this and the evanescent nature of the interaction between the mode and top cladding, 500 nm was chosen as the PMMA top cladding thickness, beyond this thickness there is no significant improvement in TDWS. The resulting TOC and TDWS for the waveguide can be found by simulation and is shown to reduce the TDWS to 6.18 pm/K for a waveguide width of 1100 nm, see Fig. 6(a) . This reduces the required temperature stability to $\pm\,32\,\text{mK}$. To achieve athermal operation, a top cladding with a more negative TOC is desired. Polyurethane acrylate (PUA) has been shown to have a TOC of $-4.2 \times 10^{-4}\text{K}^{-1}$ [43]. Using this bulk TOC value the waveguide TOC and TDWS are found by simulation for an array of PUA thickness and waveguide width values, see Fig. 6(b) . For a Si_3N_4 width of 1100 nm, the optimal PUA top cladding thickness is 480 nm and results in a TDWS of $0.2\,\text{fm}\,\text{K}^{-1}$; this would be insignificant within reasonable operating temperatures and the micro-ring resonator would effectively be insensitive to temperature changes. This could eliminate the need for active temperature control, thereby reducing the footprint, power consumption, and cost of potential devices. Polymer top cladding

layers are assumed to be planar in this simulation but in order to fabricate such a device, the conformality of the polymer cladding would have to be accounted for in the simulation or the polymer layer would have to be planarized. This will be the subject of future work.
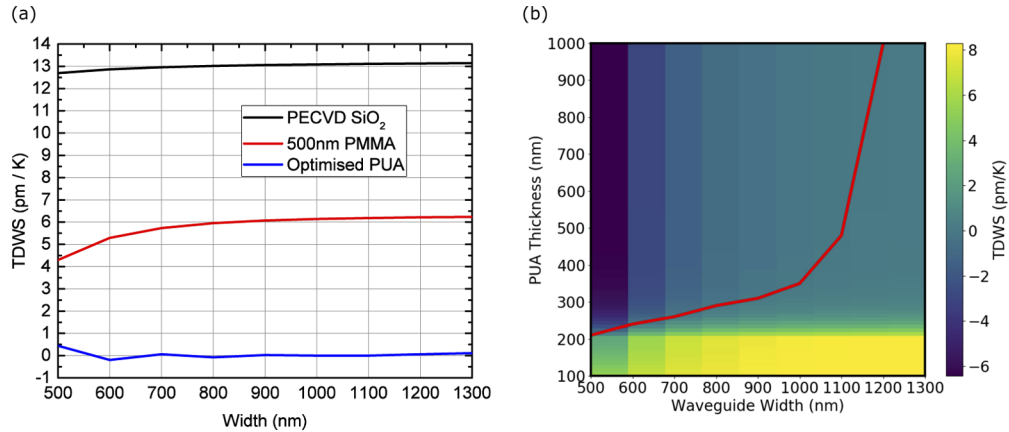
(a)   (b)

Fig. 6. The simulated temperature dependent wavelength shift (TDWS) of waveguides comprised of 200 nm LPCVD Si_3N_4 on wet thermal SiO_2 at 780 nm wavelength. (a) TDWS against waveguide width for PECVD SiO_2 top cladding (no athermalization), 500 nm polymethyl methacrylate (PMMA) top cladding, and optimized polyurethane acrylate (PUA) top cladding. (b) TDWS values shown for PUA thickness against waveguide width, optimum PUA thickness is shown by red trace.

6.   Conclusion

Micro-ring resonators have been fabricated in a 200 nm thick Si_3N_4 photonics platform with Q factors up to 1.4×10^6 at 780 nm wavelength. The thermo-optical properties of the waveguides were investigated and for a SiO_2 top cladding, a temperature dependent wavelength shift (TDWS) of 13.11 pm/K was determined indicating that a minimum temperature stability of less than $\pm$ 15 mK is required for such devices for wavelength locking applications. If a polyurethane acrylate top cladding of an optimized thickness was used, then the TDWS falls to less than 1 fm/K and the micro-ring would effectively be athermal. These results have been achieved without chemical mechanical polishing or anneals above 1100 °C which have been essential for high Q factors at 1550 nm [8,9,16]. Further optimization should therefore allow higher Q factors to be realized at a wavelength of 780 nm.

Disclosures

The authors declare no conflicts of interest.

References

1. W. Bogaerts, P. De Heyn, T. Van Vaerenbergh, K. De Vos, S. Kumar Selvaraja, T. Claes, P. Dumon, P. Bienstman, D. Van Thourhout, and R. Baets, "Silicon microring resonators," Laser Photonics Rev. **6**(1), 47–73 (2012).
2. D. T. Spencer, M. L. Davenport, T. Komljenovic, S. Srinivasan, and J. E. Bowers, "Stabilization of heterogeneous silicon lasers using Pound-Drever-Hall locking to Si_3N_4 ring resonators," Opt. Express **24**(12), 13511–13517 (2016).
3. B. Stern, X. Ji, Y. Okawachi, A. L. Gaeta, and M. Lipson, "Battery-operated integrated frequency comb generator," Nature **562**(7727), 401–405 (2018).
4. P. Del'Haye, A. Schliesser, O. Arcizet, T. Wilken, R. Holzwarth, and T. J. Kippenberg, "Optical frequency comb generation from a monolithic microresonator," Nature **450**(7173), 1214–1217 (2007).
5. D. Grassani, S. Azzini, M. Liscidini, M. Galli, M. J. Strain, M. Sorel, J. E. Sipe, and D. Bajoni, "Micrometer-scale integrated silicon source of time-energy entangled photons," Optica **2**(2), 88–94 (2015).
6. F. Dell'Olio, T. Tatoli, C. Ciminelli, and M. Armenise, "Recent advances in miniaturized optical gyroscopes," J. Eur. Opt. Soc. Rapid Publ **9**, 14013 (2014).
7. Y. Zhang, X. Hu, D. Chen, L. Wang, M. Li, P. Feng, X. Xiao, and S. Yu, "Design and demonstration of ultra-high-Q silicon microring resonator based on a multi-mode ridge waveguide," Opt. Lett. **43**(7), 1586–1589 (2018).
8. X. Ji, F. A. S. Barbosa, S. P. Roberts, A. Dutt, J. Cardenas, Y. Okawachi, A. Bryant, A. L. Gaeta, and M. Lipson, "Ultra-low-loss on-chip resonators with sub-milliwatt parametric oscillation threshold," Optica **4**(6), 619–624 (2017).
9. D. T. Spencer, J. F. Bauters, M. J. R. Heck, and J. E. Bowers, "Integrated waveguide coupled Si_3N_4 resonators in the ultrahigh-Q regime," Optica **1**(3), 153–157 (2014).
10. J. Kitching, "Chip-scale atomic devices," Appl. Phys. Rev. **5**(3), 031302 (2018).
11. S. Knappe, P. Schwindt, V. Shah, L. Hollberg, J. Kitching, L. Liew, and J. Moreland, "A chip-scale atomic clock based on ^{87}Rb with improved frequency stability," Opt. Express **13**(4), 1249–1253 (2005).
12. L. Liu, D.-S. Lü, W.-B. Chen, T. Li, Q.-Z. Qu, B. Wang, L. Li, W. Ren, Z.-R. Dong, J.-B. Zhao, W.-B. Xia, X. Zhao, J.-W. Ji, M.-F. Ye, Y.-G. Sun, Y.-Y. Yao, D. Song, Z.-G. Liang, S.-J. Hu, D.-H. Yu, X. Hou, W. Shi, H.-G. Zang, J.-F. Xiang, X.-K. Peng, and Y.-Z. Wang, "In-orbit operation of an atomic clock based on laser-cooled ^{87}Rb atoms," Nat. Commun. **9**(1), 2760 (2018).
13. J. Kitching, E. A. Donley, S. Knappe, M. Hummon, A. T. Dellis, J. Sherman, K. Srinivasan, V. A. Aksyuk, Q. Li, D. Westly, B. Roxworthy, and A. Lal, "NIST on a chip: Realizing SI units with microfabricated alkali vapour cells," J. Phys.: Conf. Ser. **723**, 012056 (2016).
14. F. P. Payne and J. P. R. Lacey, "A theoretical analysis of scattering loss from planar optical waveguides," Opt. Quantum Electron. **26**(10), 977–986 (1994).
15. F. Grillot, L. Vivien, S. Laval, D. Pascal, and E. Cassan, "Size influence on the propagation loss induced by sidewall roughness in ultrasmall soi waveguides," IEEE Photonics Technol. Lett. **16**(7), 1661–1663 (2004).
16. X. Lu, Q. Li, D. A. Westly, G. Moille, A. Singh, V. Anant, and K. Srinivasan, "Chip-integrated visible–telecom entangled photon pair source for quantum communication," Nat. Phys. **15**(4), 373–381 (2019).
17. W. H. Pernice, C. Xiong, and H. X. Tang, "High Q micro-ring resonators fabricated from polycrystalline aluminum nitride films for near infrared and visible photonics," Opt. Express **20**(11), 12261–12269 (2012).
18. C. Doolin, P. Doolin, B. C. Lewis, and J. P. Davis, "Refractometric sensing of Li salt with visible-light Si_3N_4 microdisk resonators," Appl. Phys. Lett. **106**(8), 081104 (2015).
19. T. Ling, S.-L. Chen, and L. J. Guo, "High-sensitivity and wide-directivity ultrasound detection using high Q polymer microring resonators," Appl. Phys. Lett. **98**(20), 204103 (2011).
20. C. C. Evans, C. Liu, and J. Suntivich, "Low-loss titanium dioxide waveguides and resonators using a dielectric lift-off fabrication process," Opt. Express **23**(9), 11160–11169 (2015).
21. L. Stefan, M. Bernard, R. Guider, G. Pucker, L. Pavesi, and M. Ghulinyan, "Ultra-high-Q thin-silicon nitride strip-loaded ring resonators," Opt. Lett. **40**(14), 3316–3319 (2015).
22. A. Samusenko, D. Gandolfi, G. Pucker, T. Chalyan, R. Guider, M. Ghulinyan, and L. Pavesi, "A SiON microring resonator-based platform for biosensing at 850 nm," J. Lightwave Technol. **34**(3), 969–977 (2016).
23. R. W. P. Drever, J. L. Hall, F. V. Kowalski, J. Hough, G. M. Ford, A. J. Munley, and H. Ward, "Laser phase and frequency stabilization using an optical resonator," Appl. Phys. B **31**(2), 97–105 (1983).
24. M. T. Hummon, S. Kang, D. G. Bopp, Q. Li, D. A. Westly, S. Kim, C. Fredrick, S. A. Diddams, K. Srinivasan, V. Aksyuk, and J. E. Kitching, "Photonic chip for laser stabilization to an atomic vapor with 10^{-11} instability," Optica **5**(4), 443–449 (2018).
25. K. Gallacher, R. W. Millar, D. J. Paul, F. Mirando, G. Ternent, G. Mills, and B. Casey, "Distributed feedback lasers operating at 780 nm wavelength integrated on Si substrates for chip-scale atomic systems," in *2018 IEEE 15th International Conference on Group IV Photonics (GFP)*, (2018), pp. 1–2.
26. K. Gallacher, M. Sinclair, R. W. Millar, O. Sharp, F. Mirando, G. Ternent, G. Mills, B. Casey, and D. J. Paul, "Integrated DFB lasers on Si_3N_4 photonic platform for chip-scale atomic systems," in *Conference on Lasers and Electro-Optics*, (Optical Society of America, 2019), p. STu4O7.
27. T.-H. Chang, B. M. Fields, M. E. Kim, and C.-L. Hung, "Microring resonators on a suspended membrane circuit for atom-light interactions," Optica **6**(9), 1203–1210 (2019).
28. M. Rommel, B. Nilsson, P. Jedrasik, V. Bonanni, A. Dmitriev, and J. Weis, "Sub-10nm resolution after lift-off using HSQ/PMMA double layer resist," Microelectron. Eng. **110**, 123–125 (2013).

29. M. Á. Guillén-Torres, "Feasibility of optical gyroscopic sensors in silicon-on-insulator technology," Ph.D. thesis, University of British Columbia (2015).

30. A. Freise and K. Strain, "Interferometer Techniques for Gravitational-Wave Detection," Living Rev. Relativ. **13**(1), 1 (2010).

31. W. McKinnon, D.-X. Xu, C. Storey, E. Post, A. Densmore, A. Delâge, P. Waldron, J. Schmid, and S. Janz, "Extracting coupling and loss coefficients from a ring resonator," Opt. Express **17**(21), 18971–18982 (2009).

32. B. Stern, X. Ji, A. Dutt, and M. Lipson, "Compact narrow-linewidth integrated laser based on a low-loss silicon nitride ring resonator," Opt. Lett. **42**(21), 4541–4544 (2017).

33. L. Chrostowski and M. Hochberg, *Silicon Photonics Design* (Cambridge University Press, 2015).

34. A. Yariv, "Coupled-mode theory for guided-wave optics," IEEE J. Quantum Electron. **9**(9), 919–933 (1973).

35. W.-P. Huang, "Coupled-mode theory for optical waveguides: an overview," J. Opt. Soc. Am. A **11**(3), 963–983 (1994).

36. J. F. Bauters, M. J. R. Heck, D. John, D. Dai, M.-C. Tien, J. S. Barton, A. Leinse, R. G. Heideman, D. J. Blumenthal, and J. E. Bowers, "Ultra-low-loss high-aspect-ratio Si_3N_4 waveguides," Opt. Express **19**(4), 3163–3174 (2011).

37. J. F. Bauters, M. J. R. Heck, D. D. John, J. S. Barton, C. M. Bruinink, A. Leinse, R. G. Heideman, D. J. Blumenthal, and J. E. Bowers, "Planar waveguides with less than 0.1 db/m propagation loss fabricated with wafer bonding," Opt. Express **19**(24), 24090–24101 (2011).

38. M.-C. Tien, J. F. Bauters, M. J. R. Heck, D. T. Spencer, D. J. Blumenthal, and J. E. Bowers, "Ultra-high quality factor planar si3n4 ring resonators on si substrates," Opt. Express **19**(14), 13551–13556 (2011).

39. R. L. Barger, M. Sorem, and J. Hall, "Frequency stabilization of a cw dye laser," Appl. Phys. Lett. **22**(11), 573–575 (1973).

40. V. Raghunathan, W. N. Ye, J. Hu, T. Izuhara, J. Michel, and L. Kimerling, "Athermal operation of silicon waveguides: spectral, second order and footprint dependencies," Opt. Express **18**(17), 17631–17639 (2010).

41. J. Teng, P. Dumon, W. Bogaerts, H. Zhang, X. Jian, X. Han, M. Zhao, G. Morthier, and R. Baets, "Athermal silicon-on-insulator ring resonators by overlaying a polymer cladding on narrowed waveguides," Opt. Express **17**(17), 14627–14633 (2009).

42. A. W. Elshaari, I. E. Zadeh, K. D. Jöns, and V. Zwiller, "Thermo-optic characterization of silicon nitride resonators for cryogenic photonic circuits," IEEE Photonics J. **8**(3), 1–9 (2016).

43. Z. Zhang, P. Zhao, P. Lin, and F. Sun, "Thermo-optic coefficients of polymers for optical waveguide applications," Polymer **47**(14), 4893–4896 (2006).